Contents lists available at ScienceDirect

Transactions of Nonferrous Metals Society of China

36(2026) 156−170

www.tnmsc.cn

Effects of electroshock treatment on microstructure evolution and mechanical properties of Ti−8Al−1Mo−1V alloy

Jian ZHOU [a,b#], Yu-peng YAO [a,b#], Hong-xin SUN [a,b], Chang LIU [a,b], Yan WEN [a,b,*], Li-qiang WANG [c],
Lai-chang ZHANG [d], Le-chun XIE [a,b,**], Lin HUA [a,b]

[a] Hubei Key Laboratory of Advanced Technology for Automotive Components, Wuhan University of Technology, Wuhan 430070, China;
[b] Hubei Collaborative Innovation Center for Automotive Components Technology, Wuhan 430070, China;
[c] State Key Laboratory of Metal Matrix Composites, School of Materials Science and Engineering, Shanghai Jiao Tong University, Shanghai 200240, China;
[d] Centre for Advanced Materials and Manufacturing, School of Engineering, Edith Cowan University, Joondalup, Perth, WA6027, Australia

---

Abstract: The effect mechanism of electroshock treatment (EST) on microstructure evolution and mechanical property variations of Ti−8Al−1Mo−1V alloy was investigated. The results show that EST results in the phase transformation from the acicular secondary α_s to β phase. While the EST time is 0.12 s, the acicular martensitic phase (α_M) precipitates. The results of electron backscattered diffraction (EBSD) reveals that the average grain size decreases from 3.95 to 2.53 μm after EST, indicating that the grains are refined, and the significant recrystallization behavior and martensitic transformation occur. The orientation distribution reveals a more uniform distribution of texture, which is caused by the variation of crystal orientation after the phase transformation. The compression fracture behavior of materials indicates that EST significantly enhances the yield strength while reduces the fracture strain. The improvement of yield strength is mainly attributed to the precipitation of martensitic phase. All results indicate that EST is an effective approach for manipulating the microstructure and optimizing the texture distribution of titanium alloys.

Keywords: electroshock treatment (EST); titanium alloys; grain size; texture distribution; Ti−8Al−1Mo−1V

---

1 Introduction

Titanium alloys are widely used in various fields such as petrochemicals, biomedical, and transportation due to their high specific strength and excellent corrosion resistance [1−5]. In particular, the specific strength of titanium alloys is required when the temperature exceeds 300 °C [6]. Typically, the microstructure of titanium alloys can be tuned via heat treatment and thermomechanical processes for further enhancing the mechanical properties [7]. YUMAK and ASLANTAS [8] improved the mechanical properties of metastable β titanium alloy through the application of heat treatment, such as aging treatment and cryogenic treatment. ELSHAER and IBRAHIM [9] found that the aging process following solution treatment can considerably enhance the wear resistance of TC21 alloy up to 122% compared to the annealed specimens. Heat treatment can modify the microstructure and improve the strength of titanium

---

[#] Jian ZHOU and Yu-peng YAO contributed equally to this work

Corresponding author: [*]Yan WEN, E-mail: gubi2008@whut.edu.cn; [**]Le-chun XIE, E-mail: xielechun@whut.edu.cn

https://doi.org/10.1016/S1003-6326(25)66955-X
Received 18 April 2024; accepted 17 December 2024

alloys, but these methods are time-consuming, ranging from several hours to even tens of hours [10,11].

In recent years, researchers have been attempting to find an efficient and convenient method to modify the microstructure and improve the mechanical properties. Electropulsing treatment is attracting much attention for its short duration, environmental friendliness, and non-polluting characteristics [12,13]. By accurately adjusting the current density, the microstructure optimization of materials can be achieved. The effects of electropulsing treatment on the microstructure variation of the Ti−6Al−4V (TC4) alloy have been investigated further [14−17]. GAO et al [18] have conducted the rapid hardening and softening of Ti−6Al−4V alloy under different discharge voltages by electropulsing treatment. Furthermore, it has been discovered that the refinement of grains was attributed to the ability of pulse current to reduce the thermodynamic barrier for the solid-state phase transformation from α to β. CHEN et al [19] found that electropulsing treatment could rapidly dissolve the η' phase in AA7150 Al alloy within 20 s at low temperatures. Meanwhile, the strength and ductility of the specimens sharply decreased. WU et al [20] found that the electropulsing treatment could significant enhance the dynamic recrystallization and texture evolution of Ti−6Cr−5Mo−5V−4Al alloy, while the dislocation density decreased with the increase of current density.

Electroshock treatment (EST) is similar to electropulsing treatment, and it owns the greater advantages compared to electropulsing treatment, i.e. high current density, continuous and stable pulse current, handling bulk specimens and large components, as well as achieving the targeted processing on local area. It shows more pronounced effects on the microstructure modulation and improvement in mechanical properties [21,22]. It was reported that EST can promote the transformation of the α to β phase in Ti−6.5Al−3.5Mo−1.5Zr−0.3Si alloy, reduce the volume fraction of β phase, refine the grain size of α phase, and enhance the texture strength of the α phase [23−25]. WU et al [26,27] demonstrated that the combination of EST and external loading could reduce the texture intensity of the α phase, inducing variations in interplanar spacing and the generation of defects by α phase and TiB deformation. ZHOU et al [28] demonstrated that EST could reduce prior β grain size, eliminate residual texture, and the tensile strength and elongation were both increased. Ti−8Al−1Mo−1V is near-α titanium alloy designed for manufacturing of various components in high-temperature gas turbine engines and compressor blades [29]. This near-α titanium alloy demonstrates outstanding high-temperature tensile strength, creep resistance, and thermal stability [30,31]. Previous literatures have indicated that heat treatment could adjust grain size and enhance the mechanical properties of Ti−8Al−1Mo−1V alloy [32,33]. However, using a more efficient and energy-saving approach of EST to manipulate the microstructure and mechanical properties of Ti−8Al−1Mo−1V alloy has less been studied in detail.

In this work, the microstructure evolution and the mechanical properties variation of Ti−8Al−1Mo−1V under EST have been investigated. The scanning electron microscopy (SEM) was employed to characterize the microstructure evolution. X-ray diffraction (XRD) was conducted to quantitatively analyze the phase composition. The electron backscattered diffraction (EBSD) was utilized to reveal the orientation distribution and texture evolution in Ti−8Al−1Mo−1V under the influence of EST. The results could provide new ideas and methods for the microstructure optimization and the mechanical properties modification of near-α titanium alloy.

2 Experimental

2.1 Specimen preparation and experimental procedure

The original Ti−8Al−1Mo−1V bars were produced through hot rolling, and the chemical compositions are presented in Table 1. The experimental specimens were processed into cylindrical specimens with a diameter of 5 mm and a length of 10 mm, which was clamped by two copper electrodes tightly (Fig. 1(a)). Before EST, the specimen surfaces were mechanically polished to remove the oxide layer. EST was performed using a quasi-sin waveform with a current amplitude of 4200 A and a frequency of 50 Hz, and the current density was 2.14×10^4 A/cm^2, as shown in Fig. 1(b). A triggering circuit was used to control the pulse frequency and EST time, while a Hall sensor was employed to monitor the real-time

Table 1 Chemical compositions of Ti−8Al−1Mo−1V alloy (wt.%)

Al	Mo	V	Fe	Ti
7.35−8.35	0.7−1.25	0.75−1.25	0.3	Bal.

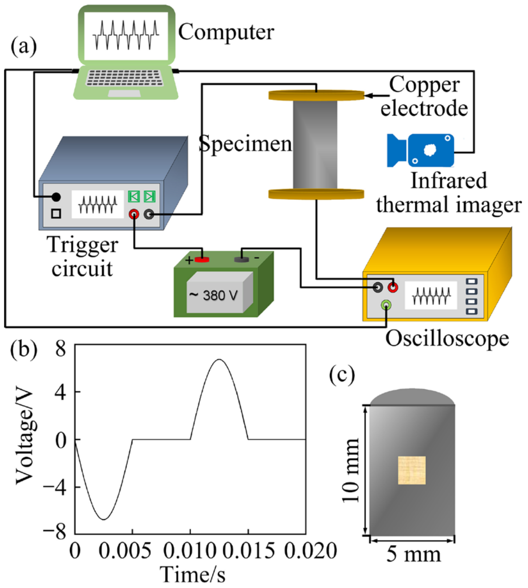

Fig. 1 (a) Schematic diagram of EST experiment; (b) Pulse waveform of EST; (c) Characterization area for SEM and EBSD

Table 2 Specimen serial number and EST time

Specimen	EST time/s
EST-0	0
EST-1	0.08
EST-2	0.10
EST-3	0.12

conditions of the pulse waveform. The infrared thermal imager (Fotric 220C) was used to collect the maximum surface temperature of specimen, and further analyze the temperature data using FotricAnalyzIR software. The correlation between pulse waveform and EST time is presented in Table 2. The room temperature compression test was conducted using a SANS-CMT5205 type compression testing machine at a compression rate of 0.2 mm/min. To ensure that the indenter could smoothly and vertically apply force to the cylindrical specimen, sandpaper was used to polish the surface of the specimen.

2.2 Microstructure characterization

The SEM was used to characterize the microstructural evolutions of the specimen. The metallographic specimens were prepared via mechanical polishing using 240, 600, 1200, and 4000 grit SiC papers in order. Then, the polishing process was carried out using a mixture of OPS suspension and H_2O_2 solution (V_{OPS}:$V_{H_2O_2}$=3:2), and the OPS solution is a suspension with the SiO_2 particle size of 40 nm. And finally, ultrasonic cleaning was performed for 5 min to ensure the cleanliness of the specimens surface. The Oxford c-nano EBSD system was utilized to analyze the orientation distribution. Before conducting EBSD characterization, the specimens were subjected to electrolytic polishing using an 8% perchloric acid and 92% ethanol mixed solution to remove the surface stress layer. The polishing voltage was set at 25 V for a duration of 20 s. Texture analysis and orientation distribution were performed using the open-source programmable toolbox Mtex version 5.8.0 in Matlab [34]. SEM and EBSD characterization regions were both located in the central region of the specimen, as shown in Fig. 1(c). The phase composition analysis was performed via PANalytical Empyrean X-ray diffraction, the scanning speed was 0.05 (°)/s and the scanning angle ranged from 30° to 90°. The operating voltage and current were 45 kV and 40 mA, respectively. Here, the four-point probe method was used to measure the resistivity variations, which was used for characterizing metals with low electrical resistivity widely. Two probes were used for measuring the current, while the other two probes measured the voltage. The resistivity was accurately calculated by taking the ratio of the voltage to the current.

3 Results and discussion

3.1 Evolution of phases structure

Figure 2 presents the microstructures of Ti−8Al−1Mo−1V alloy with different EST time. It is evident that the initial specimen shows an equiaxed grains and consists of primary α phase (dark color) and β phase (white color) (Fig. 2(a)). Further observation from high magnification reveals that, a large amount of well-defined acicular secondary α phase (α_s) is uniformly distributed in the β phase (Fig. 2(b)). These acicular α_s phases are of HCP (hexagonal close packed) structure, hindering the movement of the dislocations and enhancing the resistance to crack propagation of the

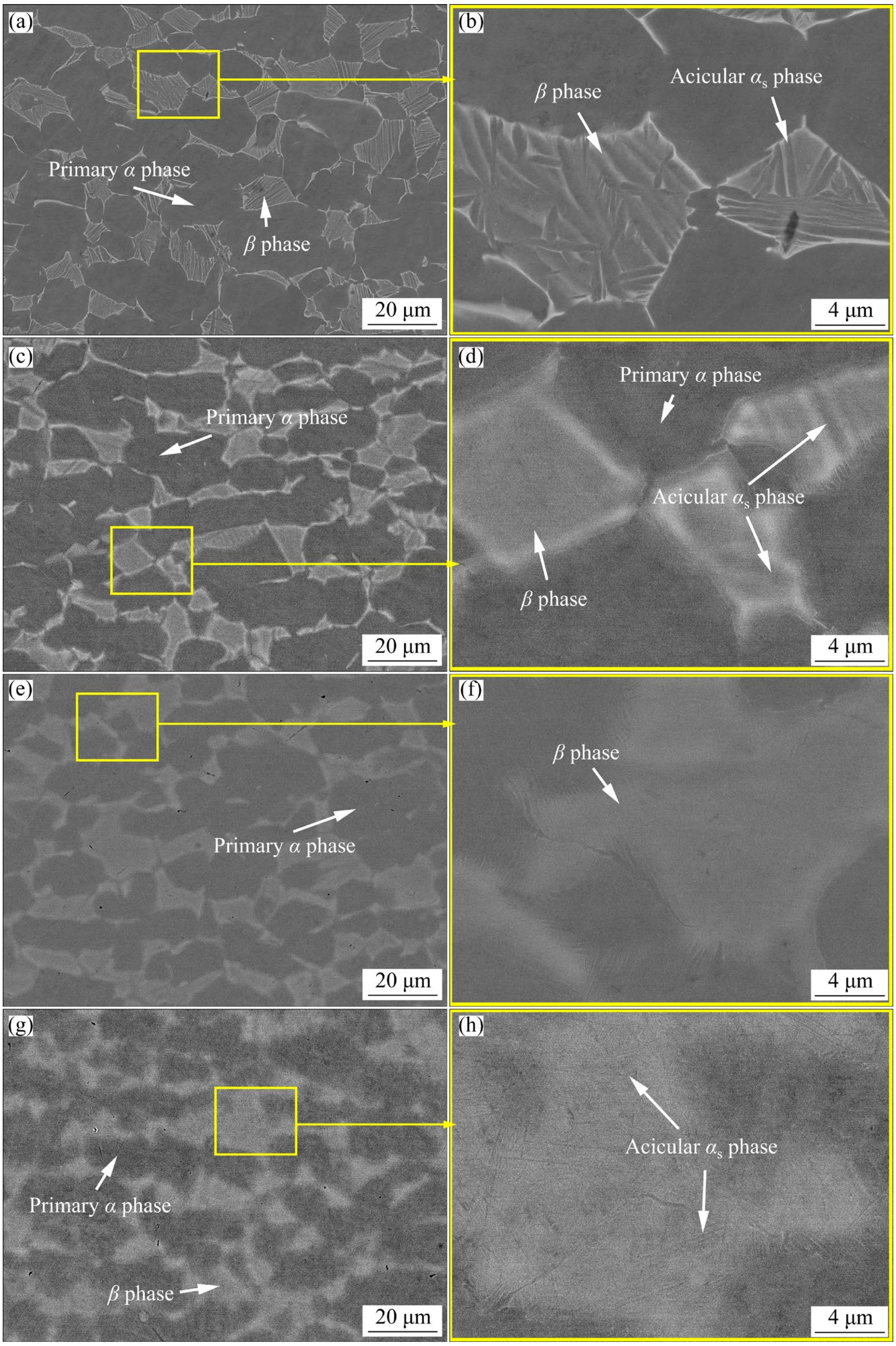

Fig. 2 Microstructures of specimens with different EST time: (a, b) EST-0; (c, d) EST-1; (e, f) EST-2; (g, h) EST-3

material. After 0.08 s of EST, the microstructure of the specimen shows an equiaxed morphology (Fig. 2(c)). Other images reveal that the phase boundaries between *α* and *β* phase are unclear, and meanwhile, the quantity of α_s phase is reduced (Fig. 2(d)), due to the local phase transformation from the α_s to *β* phase during EST. When the EST time increases to 0.1 s, although it still maintains an equiaxed structure (Fig. 2(e)), the α_s phase disappears completely, the interface of *β* phase is smooth and flat, and the boundary between the *α* and *β* phases is indistinct (Fig. 2(f)). While the EST time reaches 0.12 s, both the *α* and *β* phases show blurry (Fig. 2(g)). Due to the rapid cooling rate, the acicular martensitic phase (α_M) precipitates within the β phase (Fig. 2(h)).

The XRD results can effectively validate the evolution process of the phase structure, as shown in Fig. 3. After EST, all diffraction peaks of the α phase can be clearly observed, whereas the diffraction peaks of β phase are significantly weakened. Especially, the diffraction peak of β(101) lattice plane nearly disappears for EST-3 (Fig. 3(a)). Moreover, the diffraction peaks of the α phase in the EST specimens are significantly broader compared to EST-0, and the main contributors may be the increased dislocation density, and the micro-strain [35]. According to the Scherrer formula [36], the relation between the broadening of diffraction peaks and the grain size can be described as follows:

$$D=\frac{K\gamma}{B\cos\theta} \tag{1}$$

$$\varepsilon=\frac{B}{4\tan\theta} \tag{2}$$

where D is the grain size, K is the shear modulus, γ is the X-ray wavelength, B represents the full width at half maximum (FWHM) of diffraction peak, θ is the Bragg diffraction angle, and ε is the microstrain. At the same diffraction peak position, the grain size is inversely proportional to the FWHM of diffraction peak. The diffraction peaks of the α phase are analyzed using MDI Jade 6, as shown in Fig. 3(b). Compared to EST-0, the FWHM values of the $(10\bar{1}0)$, (0001), and $(11\bar{2}0)$ diffraction peaks are all increased. According to Eq. (2), this result indicates the increase in microstrain after EST.

Figure 4(a) shows the maximum temperature of the specimen surface measured by an infrared thermal imager. The high temperatures induce the generation of martensite phases in EST-3, which can be observed in Fig. 2(f). The resistivity is strongly correlated with the crystal structure [37−39]. Figure 4(b) illustrates that the resistivity is initially decreased and then increased after EST. The average resistivity of EST-0 is 1.94 μΩ·m. For EST-1, EST-2, and EST-3, the average resistivity

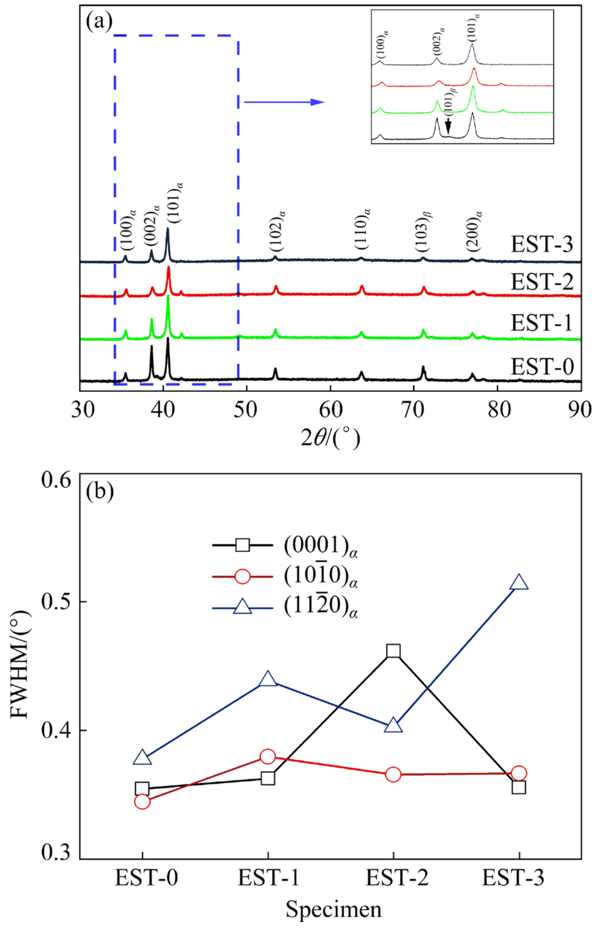

Fig. 3 (a) XRD patterns and (b) FWHM variations for different specimens

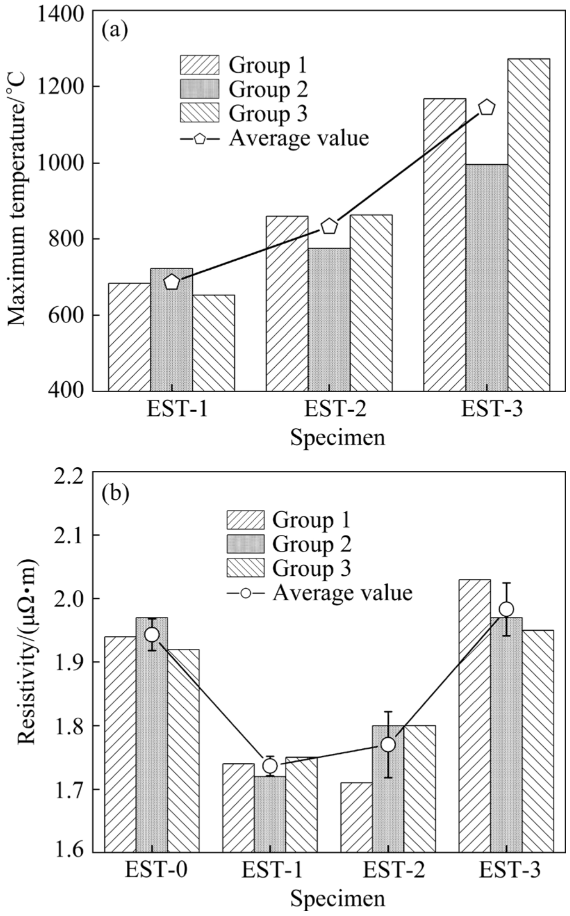

Fig. 4 Variations of (a) maximum temperature and (b) resistivity of specimens

values are 1.74, 1.77 and 1.98 μΩ·m, respectively. The electrical resistivity is highly sensitive to phase composition, and moreover, it is closely correlated with the content of each phase. The variations of electrical resistivity after EST is caused by the occurrence of phase transformation and the precipitation of martensitic phases. Meanwhile, phase transformation is typically accompanied by volume variations and an increase in residual stress. The lattice distortion caused by residual stress can further induce an increase in resistivity [40].

3.2 Variation of grain size and grain boundaries

Figure 5 shows the inverse pole figure (IPF) maps of the central region in specimens. It is clearly revealed that the initial specimen possesses an equiaxed grains with no distinct specific orientation (Fig. 5(a)). After EST with 0.08 s, there is no obvious variations in both grain structure and grain orientation (Fig. 5(b)). With the increase of EST time, the grain shape shows irregularity (Figs. 5(c, d)). To further investigate the effect of EST on grain boundaries and grain size, the distribution of grain boundary and the statistics of grain size are shown in Fig. 6. Generally, the grain boundaries can be classified into high-angle grain boundaries (HAGBs) and low-angle grain boundaries (LAGBs) based on the grain boundaries misorientation angles (θ). Here, HAGBs ($\theta > 5°$) are shown as black lines, while LAGBs ($2° \le \theta \le 15°$) are marked as red lines. It can be intuitively seen from Figs. 6(a−d) that there is a significant increase in the quantity of grain boundary after EST. This indicates that EST contributes to the grain boundary migration.

The statistics of grain boundary misorientation angles further reveals that the grain boundaries of all specimens show the strongest peaks close to 2° and 60° (Figs. 6(i−l)) correspond to the orientation angles of equiaxed α phase and acicular α_s phase, respectively. After EST with 0.08 s, the peak near 30° shows a significant enhancement; however, the strongest peak shifts from 30° to 60° for EST-2 and EST-3, and this phenomenon may be attributed to the precipitation of the acicular martensite (α_M phase) during cooling process [24]. The relative frequency curve and cumulative frequency curve of grain size distribution are shown in Figs. 6(i−l), fitted with the lognormal function and the ExpAssoc function [41], respectively. After EST, there is a decrease in d_{90}, d_{50}, and d_{10}, especially for d_{90}, which decreases from 12.42 μm in EST-0 to 7.29 μm in EST-3. This indicates a significant reduction in the number of large grains, suggesting the possibility of recrystallization during EST.

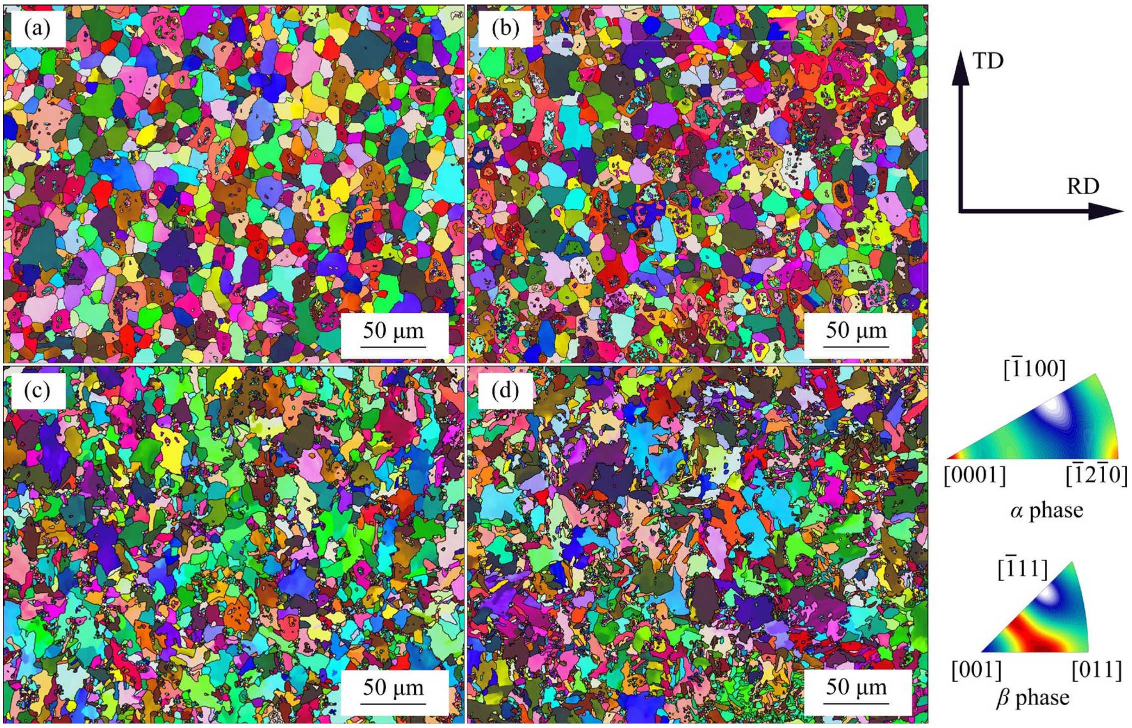

Fig. 5 IPF maps of different specimens: (a) EST-0; (b) EST-1; (c) EST-2; (d) EST-3

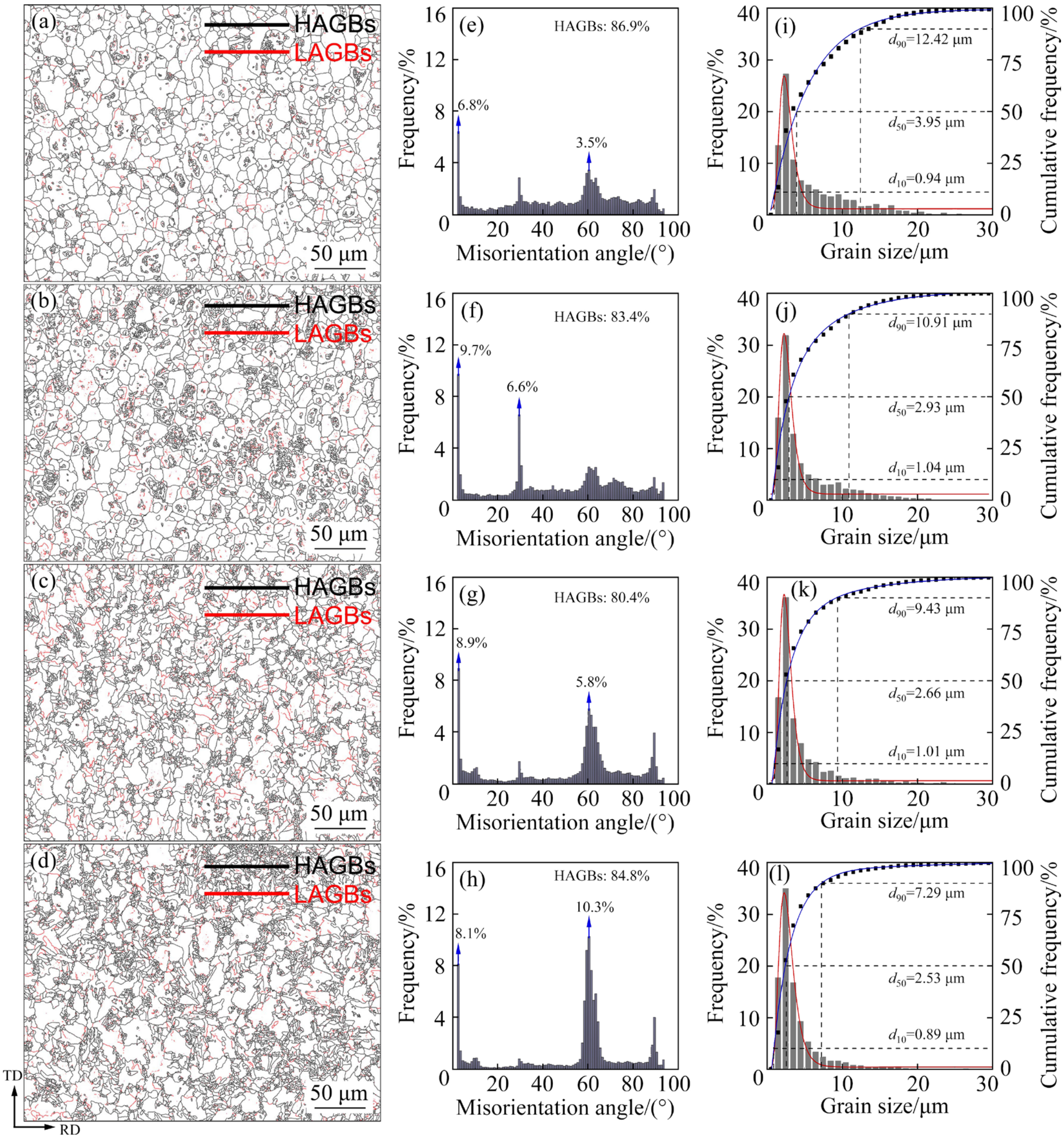

Fig. 6 (a−b) Misorientation angle distribution, (e−h) statistics maps of misorientation angle and (i−l) grain size distribution: (a, e, i) EST-0; (b, f, j) EST-1; (c, g, k) EST-2; (d, h, l) EST-3 (d_{90}, d_{50}, and d_{10} mean the grain sizes corresponding to the cumulative frequency distributions of 90%, 50%, and 10%, respectively)

3.3 Recrystallization statistics

The grain orientation spread (GOS) is employed to further explain the evolution of grain distribution after EST. GOS values reflect the average orientation of the grains [42]. In general, the distinction between the recrystallized grains and the deformed grains is based on GOS thresholds of 2° and 7°. Specifically, the low GOS values mean that the recrystallized grains appear (GOS≤2°), while the high GOS values indicate that the deformed grains are formed (GOS>7°). In contrast, the remaining grains are substructural grains (2°<GOS≤7°), as shown in Figs. 7(a−d). Before EST, mostly grains are equiaxed grains. Table 3 presents the detailed statistics of recrystallized grains. After EST, the number of recrystallized grains increases while the average diameter of grains decreases. It can be inferred that EST contributes to the grain boundary migration, and promotes the generation of small grains. The thermal and athermal effects induced by EST could enhance the nucleation rate of recrystallized grains, thereby promoting their nucleation and growth. This process provides sufficient driving force for recrystallization, resulting in an increased number of the recrystallized grains [43,44]. Figures 7(e−h) further illustrate the distribution of GOS values with respect to grain radius. It is demonstrated that

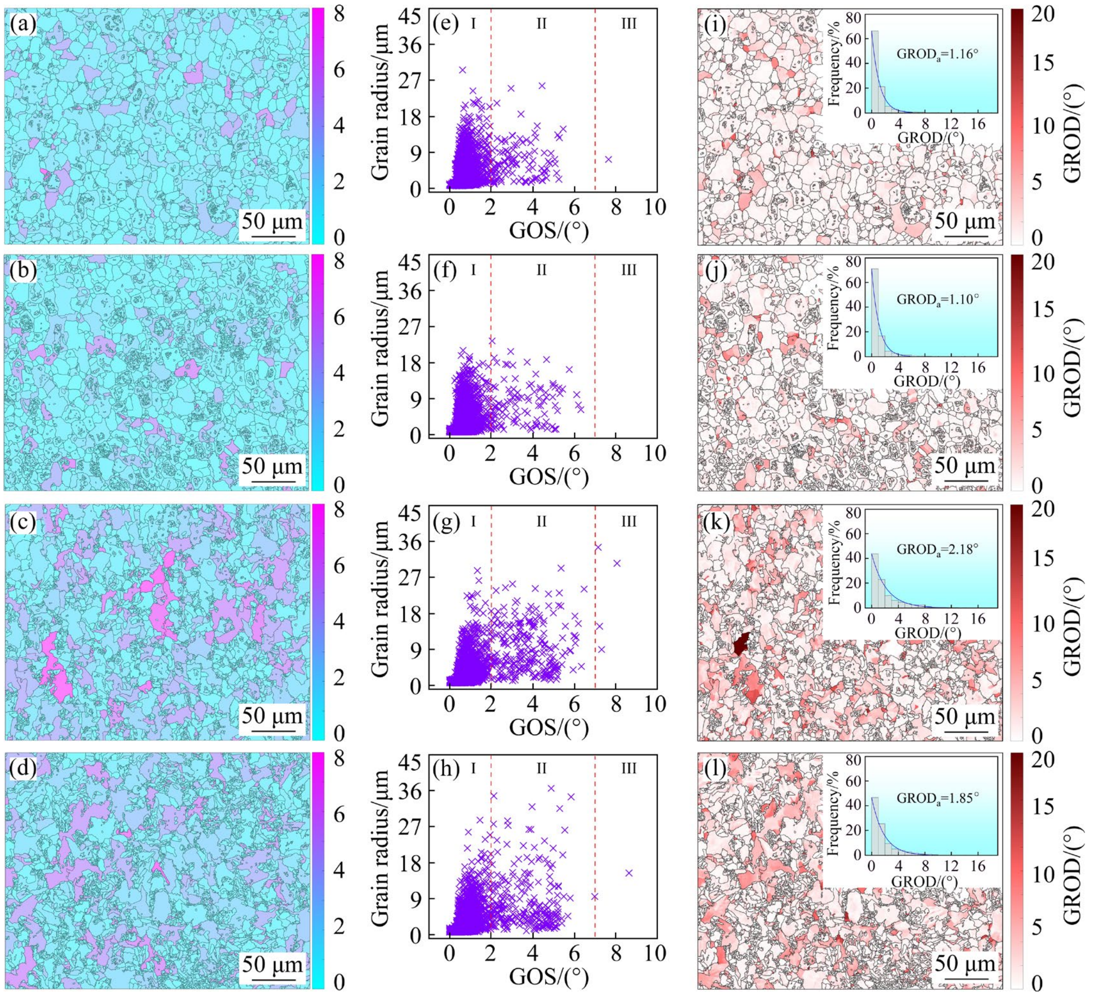

Fig. 7 (a−d) GOS distribution maps, (e−h) GOS statistical maps and (i−l) GROD distribution maps of different specimens: (a, e, i) EST-0; (b, f, j) EST-1; (c, g, k) EST-2; (d, h, l) EST-3 (The region I represents the recrystallized grains region, the region II represents the substructure region, and the region III represents the deformed grains region)

Table 3 Statistics of recrystallized grains

Specimen	Total number of grains	Number of recrystallized grains	Average diameter of recrystallized grains/μm
EST-0	2950	2839	6.2
EST-1	4447	4341	5.2
EST-2	4757	4503	4.94
EST-3	5988	5740	4.76

there is nonlinearity relation between GOS values and grain size. Meanwhile, the number of substructure grains increases after EST, which may exist a certain quantity of subgrain boundaries and dislocations in the substructure grains.

The grain reference orientation deviation (GROD) illustrates the orientation heterogeneities, making it an ideal tool to quantify internal strain during the martensitic transformation [42,45]. Generally, GROD map shows the localized orientation heterogeneities within different parts of a grain and reflects the strain distribution inside the grain [46]. Each pixel in a given grain is colored based on its misorientation to the reference orientation. By definition, the local $\mathrm{GROD}_{(i,j)}$ can be considered as the misorientation $\Delta\theta(o_{(i,j)}, o_g)$ between the orientation $o_{(i,j)}$ at position (i,j) and the reference orientation o_g of the grain the position (i,j) [47], as shown in Eq. (3):

$$\mathrm{GROD}_{(i,j)} = S_{(i,j)} \cdot \Delta\theta(o_{(i,j)}, o_g) \tag{3}$$

where $S_{(i,j)}$ is chosen to minimize the misorientation $\Delta\theta(o_{(i,j)}, o_g)$. The calculation of $\Delta\theta(o_{(i,j)}, o_g)$ can be referred to the literature [48]. From Figs. 7(i−l), after EST, the GROD map shows an uneven distribution of GROD values for each grain, with an increase in the average GROD value ($\mathrm{GROD_a}$), indicating that the specimen has a noticeable increase of internal strain compared to the EST-0. The potential reason for this significant variation could be the pressure force during EST.

3.4 Texture evolution

Figure 8 shows the pole figures (PFs) of the α phase in Ti−8Al−1Mo−1V before and after EST. It is clear that there is a texture in the {0001} planes parallel to the RD axis for EST-0 and EST-1. However, the texture of the α phase appeared along the {0001} planes parallel to the TD axis for both EST-2 and EST-3, forming the maximum texture intensity of 5.8 in EST-2. After EST, the maximum texture intensity exhibits a decreasing trend along the $\{10\bar{1}0\}$ planes, while there is no significant variation in the $\{11\bar{2}0\}$ planes. The highest intensity peaks splits from two clusters to multiple clusters, exhibiting rotational symmetry along the ND direction for EST-2 and EST-3. The inverse pole figure (IPFs) in Fig. 9 clearly indicates that the EST-0 specimen exhibits a preferred orientation along the {0001} planes, with a maximum texture intensity of 3.8, which aligns with the rolling direction. In EST-1, the preferred orientation is parallel to the TD direction, and the maximum texture intensity is reduced to 2.4. When continuing to increase the EST time, the preferred orientation direction of EST-2 and EST-3 becomes parallel to the RD axis ({0001} planes), and the crystal orientation becomes dispersed based on the oriented nucleation theory and oriented growth theory [49]. By adjusting the time of EST, it is possible to adjust the phase transformation behavior at different stages ($\alpha \rightarrow \beta$ or $\beta \rightarrow \alpha_M$), further achieving the variation in texture. It is revealed that EST can significantly optimize texture and orientation distribution.

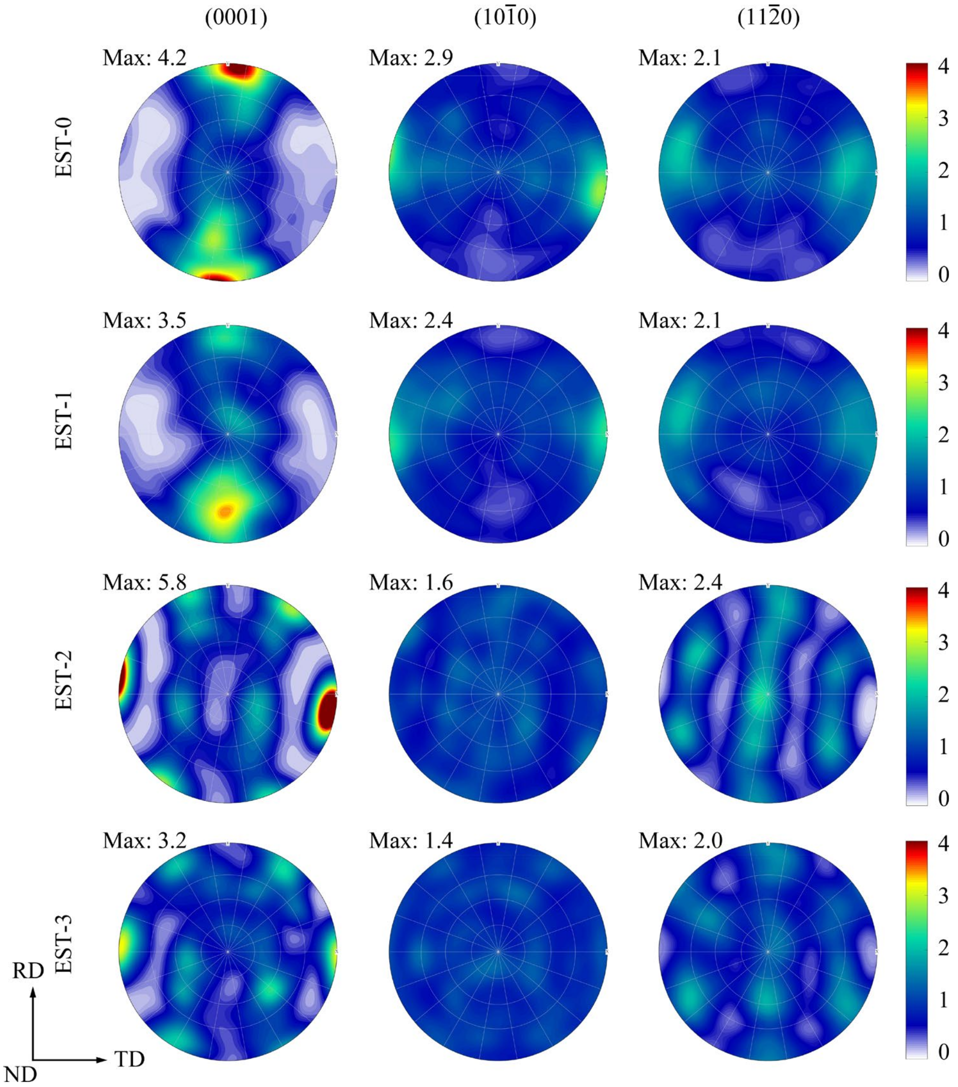

Fig. 8 Pole figures of α phase in different specimens

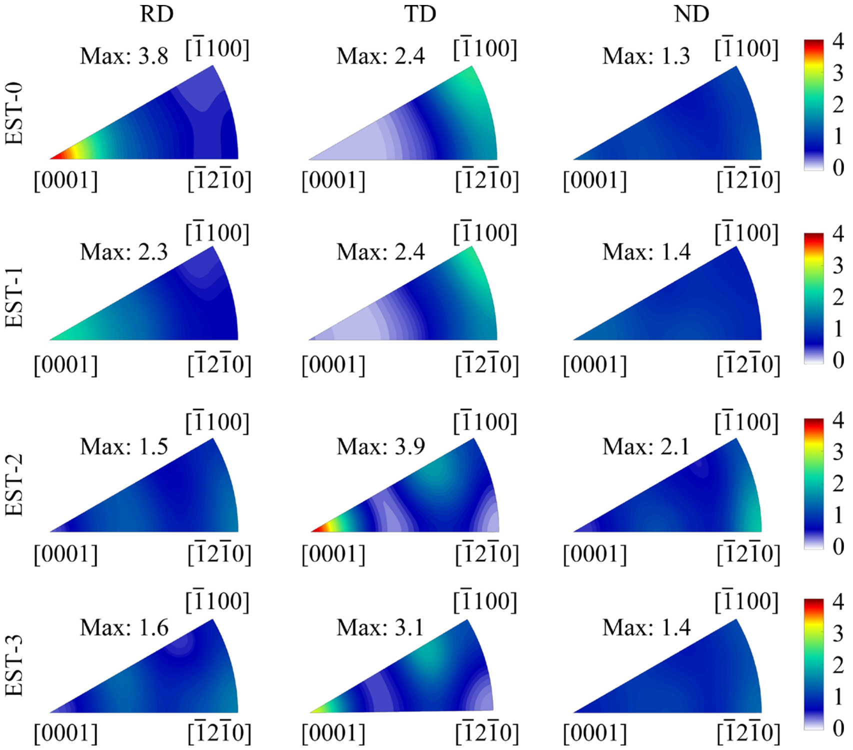

Fig. 9 Inverse pole figures of *α* phase of different specimens

3.5 Mechanical properties

According to the stress−strain curve obtained from the compression experiment at room temperature (Fig. 10(a)), the yield strength and the fracture strain of specimens are depicted in Fig. 10(b). It can be seen that for EST-0, the specimen exhibits a fracture strain of 52.72% and a yield strength of 801 MPa. With increasing the EST time, the yield strength increases while the fracture strength decreases. For EST-2, the yield strength increases to 1049 MPa, while the fracture strain decreases to 34.86%. The main reason is that the precipitation of martensite significantly enhances the mechanical properties of the material. Besides, the precipitation of martensitic phases causes lattice distortions and increases internal stresses in the material [50]. The martensitic microstructure itself exhibits exceptionally high hardness and strength, which effectively hinders dislocation motion and further enhances the yield strength of the material [51]. There are four strengthening mechanisms for titanium alloys and metal materials, including thesolid solution strengthening, the dislocation strengthening, the grain boundary strengthening, and the precipitation strengthening [52]. Due to the reduction in grain diameter, the increase in the number of grain boundaries, and the precipitation of the martensite phase, the improvement in mechanical properties can be attributed to the grain boundary strengthening and the precipitation strengthening [53−55].

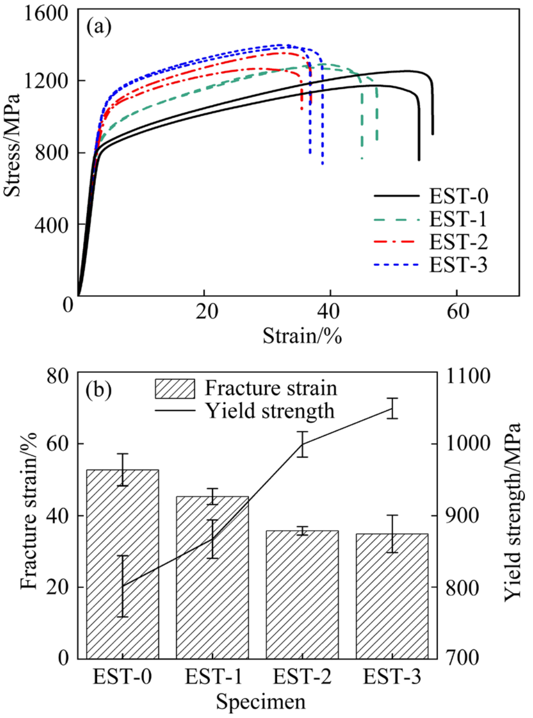

Fig. 10 (a) Compressive stress−strain curves; (b) Variation of fracture strain and yield strength

In order to show the effect of EST on the compressive fracture behavior of the specimen, the fracture morphologies are characterized and analyzed (Fig. 11). It is intuitively obvious that there exist large areas of dimples and fluvial shape in EST-0 (Figs. 11(a, b)), which may be attributed to shear stress generated during the compression process. In EST-1, the certain dimples and fluvial shape appear, accompanied by more smooth surface (Figs. 11(c, d)). When continuing to increase the EST time, there are few dimples and fluvial shape, while smooth surface becomes obvious. It is indicated that the predominant fracture mode is ductile fracture for EST-0. However, after EST, the fracture mode is primarily a mixture of ductile fracture and brittle fracture. All results indicate that EST can modify the microstructure effectively and improve the mechanical properties.

3.6 Discussion

The effect mechanism of EST on the microstructure evolution is indicated in Fig. 12. The initial specimen is mainly composed of a dual-phase structure, comprising an acicular α_s phase and β phase (Fig. 12(a)). When the current passes through the α_s phase, the thermal effect causes the increase of temperature (Fig. 12(b)). Due to the difference in resistivity between the α_s and β phases, the non-uniform distribution of the current leads to thermal concentration at the tip of the α_s phase (Fig. 12(c)). Once the temperature exceeds the phase transition temperature, the α_s

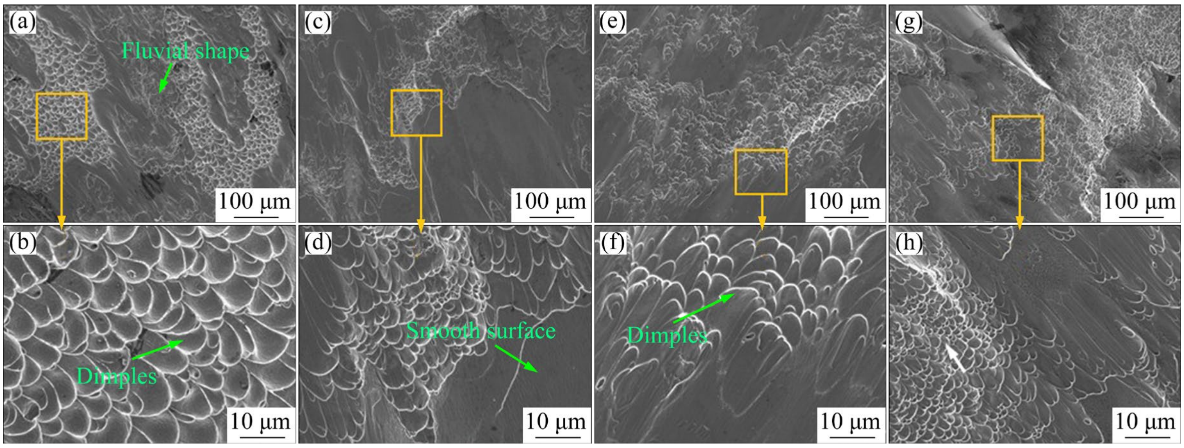

Fig. 11 Compression fracture morphologies of specimens: (a, b) EST-0; (c, d) EST-1; (e, f) EST-2; (g, h) EST-3

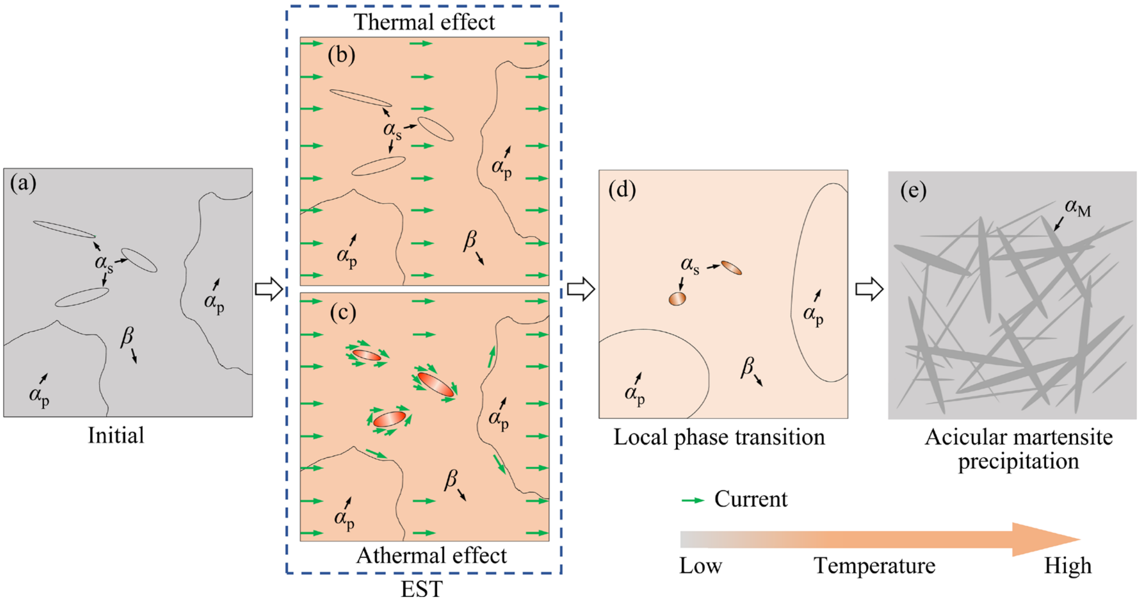

Fig. 12 Microstructural evolution induced by EST: (a) Initial state; (b) Current flowing through α_s and β phases; (c) Heat concentration at tip of α_s phase; (d) Local phase transition; (e) Precipitation of acicular martensite phase α_M

phase transforms into the β phase, and the acicular α_s phase shows significant decrease (Fig. 12(d)), which reveals that the α_s phase appears blurred. During the cooling process, the α_M martensite phase is precipitated and the α_M phases have a high aspect ratio and are distributed within the β phase (Fig. 12(e)). Furthermore, the α_M phase exhibits a noticeable promoting effect on the enhancement of yield strength.

4 Conclusions

(1) The microstructure of the specimen before EST includes the α phase, β phase, and acicular α_s phase. After EST, the α_s phase content decreases. With the increase in EST time to 0.12 s, the acicular martensitic phases (α_M) precipitate within the β phase.

(2) After EST, the grain size and the proportion of high-angle grain boundaries both decrease. The misorientation angles show the high concentration near 60°. The recrystallization occurs.

(3) After EST, the distribution of texture becomes more uniform. The maximum texture intensity shows a decreasing trend along the $\{10\bar{1}0\}$ planes, while there is no significant variation in the $\{11\bar{2}0\}$ planes. This is mainly attributed to the fact that the phase transformation behavior influences the grain orientation during grain nucleation and growth.

(4) After EST, the yield strength significantly increases, and the fracture mode is changed from the plastic fracture to the combination of plastic fracture and ductile fracture, which is closely related to the precipitation of martensitic phase.

(5) Owing to the difference in resistivity between the α_s and β phase, the non-uniform distribution of current induces the localized energy concentration at the tip of the α_s phase, which causes the transformation of the α_s into the β phase. As the temperature surpasses the phase transition temperature, the α_M phase precipitates during the cooling process after EST. The precipitation of α_M contributes to strengthening the mechanical properties of Ti−8Al−1Mo−1V alloy.

CRediT authorship contribution statement

Jian ZHOU: Investigation, Data curation, Writing − Original draft; **Yu-peng YAO:** Writing − Review & editing; **Hong-xin SUN:** Writing − Review & editing; **Chang LIU:** Writing − Review & editing; **Yan WEN:** Writing − Review & editing; **Li-qiang WANG:** Writing − Review & editing; **Lai-chang ZHANG:** Writing − Review & editing; **Le-chun XIE:** Methodology, Writing − Original draft, Writing − Review & editing; **Lin HUA:** Supervision, Methodology, Writing − Review & editing.

Declaration of competing interest

The authors declare that they have no known competing financial interests or personal relationships that could have appeared to influence the work reported in this paper.

Data availability

The data that support the findings of this study are available from the corresponding author upon reasonable request.

Acknowledgments

This work was financially supported by the National Key R&D Program of China (No. 2020YFA0714900), Major Research Plan of the National Natural Science Foundation of China (No. 92266102), the National Natural Science Foundation of China (Nos. 52271135, 52433016), the Innovation Funding Project of National Engineering and Research Center for Commercial Aircraft Manufacturing, China (No. COMAC-SFGS-2022-1871), the Overseas Expertise Introduction Project for Discipline Innovation, China (No. B17034), and the Innovative Research Team Development Program of Ministry of Education of China (No. IRT_17R83).

References

[1] ZHANG Lai-chang, CHEN Liang-yu. A review on biomedical titanium alloys: Recent progress and prospect [J]. Advanced Engineering Materials, 2019, 21: 1801215.

[2] TAN Chao-lin, WENG Fei, SUI Shang, CHEW Y X, BI Gui-jun. Progress and perspectives in laser additive manufacturing of key aeroengine materials [J]. International Journal of Machine Tools and Manufacture, 2021, 170: 103804.

[3] SU Jin-long, JIANG Fu-lin, TENG Jie, CHEN Le-qun, YAN Ming, REQUENA G, ZHANG Lai-chang, WANG Y M, OKULOV L V, ZHU Hong-mei. Recent innovations in laser additive manufacturing of titanium alloys [J]. International Journal of Extreme Manufacturing, 2024, 6: 032001.

[4] YANG Jun-wei, TANG Hai-bo, WEI Pei-yuan, GAO Hong-wei, WANG Jia-wei, HUO Hai-xin, ZHU Yan-yan. Microstructure and mechanical properties of an ultrahigh-strength titanium alloy Ti−4.5Al−5Mo−5V−6Cr−1Nb prepared using laser directed energy deposition and forging: a comparative study [J]. Chinese Journal of Mechanical

Engineering: Additive Manufacturing Frontiers, 2023, 2: 100064.

[5] YUAN Bao-guo, QIAN De-guo, ZHANG Xiao-xue, QIANG CHEN, TANG Ai-chuang. Microstructure and room-temperature mechanical property of TC21 alloy treated by continuous multistep hydrogenation at different temperatures [J]. Transactions of Nonferrous Metals Society of China, 2024, 34: 1520−1532.

[6] LIANG Xiao-liang, LIU Zhan-qiang, YAO Gong-hou, WANG Bing, REN Xiao-ping. Investigation of surface topography and its deterioration resulting from tool wear evolution when dry turning of titanium alloy Ti−6Al−4V [J]. Tribology International, 2019, 135: 130−142.

[7] DIXIT S, DASH B B, KUMAR D, BHATTACHARJEE A, SANKARAN S. Influence of phase morphology, static recrystallization, and crystallographic texture on room temperature tensile properties of Ti−6Al−4V alloy: Comparison between post-tested equiaxed, bimodal, and lamellar microstructures [J]. Materials Science and Engineering A, 2023, 873: 144990.

[8] YUMAK N, ASLANTAS K. A review on heat treatment efficiency in metastable β titanium alloys: The role of treatment process and parameters [J]. Journal of Materials Research and Technology, 2020, 9: 15360−15380.

[9] ELSHAER R N, IBRAHIM K M. Effect of cold deformation and heat treatment on microstructure and mechanical properties of TC21 Ti alloy [J]. Transactions of Nonferrous Metals Society of China, 2020, 30: 1290−1299.

[10] RONG Ran, YANG Wang, REN Fu-qiang, ZHANG Yuan-xiang, FENG Fang, ZHANG Wei-na, GUO Yuan, WANG Guo-dong. Ultra-high strength Inconel 718 alloy produced by a novel heat treatment [J]. Transactions of Nonferrous Metals Society of China, 2024, 34: 2204−2218.

[11] DANG Zong-yu, QIN Guo-liang, HONG Ma, GENG Pei-hao. Multi-scale characterizations of microstructure and mechanical properties of Ti6242 alloy linear friction welded joint with post-welded heat treatment [J]. Transactions of Nonferrous Metals Society of China, 2023, 33: 1114−1123.

[12] LU Zi-chuan, GUO Chun-huan, LI Peng, WANG Zhen-qiang, CHANG Yun-peng, TANG Guo-yi, JIANG Feng-chun. Effect of electropulsing treatment on microstructure and mechanical properties of intermetallic Al3Ti alloy [J]. Journal of Alloys and Compounds, 2017, 708: 834−843.

[13] LI Guo-dong, WANG Lei, LIU Yang, ZHANG Wei, QIAO Xue-ying, WANG Yan-qing. Effects of high density electropulsing treatment on aging kinetics of GH4199 alloy [J]. Rare Metal Materials and Engineering, 2011, 40: 961−966.

[14] LI Gang, XIAO Xin-lei, ZHANG Wen-kang, SONG Da. Effect of electropulsing-assisted ultrasonic strengthening on fatigue properties of HIP Ti−6Al−4V alloy [J]. Metallurgical and Materials Transactions A, 2023, 54: 3912−3927.

[15] YAN Xu-dong, XU Xiao-feng, WU Chao, ZHAO Yang, LI Dong-dong, ZHOU Ya-chong, WU Zhi-cheng, WEI Lai. A novel electropulsing treatment to improve the surface strength and repair the pore of additively manufactured Ti−6Al−4V alloy [J]. Surface and Coatings Technology, 2023, 458: 129364.

[16] YAN Xu-dong, XU Xiao-feng, ZHOU Ya-chong, WU Zhi-cheng, WEI Lai, ZHANG Da-yong. Surface electropulsing-induced texture evolution in electron beam melted Ti−6Al−4V alloy for biomedical application [J]. Surface and Coatings Technology, 2024, 479: 130509.

[17] YAN Xu-dong, XU Xiao-feng, ZHOU Ya-chong, WU Zhi-cheng, WEI Lai, ZHANG Da-yong. Constructing a novel bi-lamellar microstructure in selective laser melted Ti−6Al−4V alloy via electropulsing for improvement of strength and corrosion resistance [J]. Journal of Materials Science & Technology, 2024, 193: 37−50.

[18] GAO J B, BEN D D, YANG H J, MENG L X, JI H B, LIAN D L, CHEN J, YI J L, WANG L, LI P. Effects of electropulsing on the microstructure and microhardness of a selective laser melted Ti6Al4V alloy [J]. Journal of Alloys and Compounds, 2021, 875: 160044.

[19] CHEN Kai, ZHAN Li-hua, YU Wen-fang. Rapidly modifying microstructure and mechanical properties of AA7150 Al alloy processed with electropulsing treatment [J]. Journal of Materials Science & Technology, 2021, 95: 172−179.

[20] WU Chuan, ZHOU Yu-jie, LIU Bin. Experimental and simulated investigation of the deformation behavior and microstructural evolution of Ti6554 titanium alloy during an electropulsing-assisted microtension process [J]. Materials Science and Engineering A, 2022, 838: 142745.

[21] SONG Yan-li, WANG Zhong-qi, YU Yong-qing, WU Wen-lin, WANG Zhong-mei, LU Jue, SUN Qian, XIE Le-chun, HUA Lin. Fatigue life improvement of TC11 titanium alloy by novel electroshock treatment [J]. Materials & Design, 2022, 221: 110902.

[22] LI Yun-feng, WANG Fang-lei, SUN Qian, QIAN Dong-sheng, SONG Yan-li, HUA Lin. Study on the microstructure and impact toughness of TC11 titanium alloy by a novel electromagnetic shocking treatment [J]. Materials Science and Engineering A, 2023, 876: 145149.

[23] XIE Le-chun, LIU Chang, SONG Yan-li, GUO Hao-jie, WANG Zhong-qi, Lin HUA, WANG Li-qiang, ZHANG Lai-chang. Evaluation of microstructure variation of TC11 alloy after electroshocking treatment [J]. Journal of Materials Research and Technology, 2020, 9: 2455−2466.

[24] ZHOU Jian, LIU Chang, WU Ya-ya, XIE Le-chun, YIN Fei, QIAN Dong-sheng, SONG Yan-li, WANG Li-qiang, ZHANG Lai-chang, HUA Lin. Evolution mechanism of grain orientation and texture distribution of Ti−6.5Al−3.5Mo−1.5Zr−0.3Si alloy under electroshocking treatment [J]. Journal of Materials Research and Technology, 2023, 25: 5693−5704.

[25] LIU Chang, XIE Le-chun, QIAN Dong-sheng, HUA Lin, WANG Li-qiang, ZHANG Lai-chang. Microstructure evolution and mechanical property response of TC11 titanium alloy under electroshock treatment [J]. Materials & Design, 2021, 198: 109322.

[26] WU Ya-ya, WEN Yan, GUO An-an, ZHOU Jian, YIN Fei, XIE Le-chun, WANG Li-qiang, HUA Lin, LU Wei-jie, ZHANG Lai-chang. Grain boundary and texture evolution of TiB/Ti−2Al−6Sn titanium matrix composite under electroshocking treatment [J]. Journal of Materials Research and Technology, 2023, 27: 4305−4316.

[27] XIE Le-chun, WU Ya-ya, YAO Yu-peng, HUA Lin, WANG Li-qiang, ZHANG Lai-chang, LU Wei-jie. Refinement of TiB reinforcements in TiB/Ti−2Al−6Sn titanium matrix composite via electroshock treatment [J]. Materials Characterization, 2021, 180: 111395.

[28] ZHOU Ya-chong, XU Xiao-feng, ZHAO Yang, YAN Xu-dong, WEI Lai, WU Zhi-cheng, YU Yong-qiang. Achieving recrystallization of prior β in Ti−6Al−4V alloy by electroshock [J]. Journal of Alloys and Compounds, 2023, 968: 172330.

[29] XIE Yong, YAN Zhen-yu, NI Jiang-tao, DONG Peng, LI Quan, LIANG Xiao-kang, ZHOU Qing-jun, WANG Fu-de, WANG Guo-qing. Interface stability homogeneity of large-scale laser-melting-deposited titanium alloy components [J]. Additive Manufacturing Frontiers, 2024, 3: 200121.

[30] WEN Han, LI Fu, CHEN Hai-yan. Effect of welding speed on fatigue properties of TC18 thick plate by electron beam welding [J]. Rare Metal Materials and Engineering, 2018, 47: 2335−2340.

[31] ZHAO Guo-long, ZHAO Biao, DING Wen-feng, XIN Lian-jia, NIAN Zhi-wen, PENG Jian-hao, HE Ning, XU Jiu-hua. Nontraditional energy-assisted mechanical machining of difficult-to-cut materials and components in aerospace community: A comparative analysis [J]. International Journal of Extreme Manufacturing, 2024, 6: 022007.

[32] SHI Xiao-hui, ZENG Wei-dong, LONG Yu, ZHU Yan-chun. Microstructure evolution and mechanical properties of near-α Ti−8Al−1Mo−1V alloy at different solution temperatures and cooling rates [J]. Journal of Alloys and Compounds, 2017, 727: 555−564.

[33] SZKLINIARZ A. Effect of heat treatment on the microstructure and properties of Ti−8Al−1Mo−1V alloy with carbon addition [J]. Solid State Phenomena, 2015, 229: 131−136.

[34] SCHMITT M M, SAVAGE D J, YEAGER J D, WENK H R, LUTTEROTTI L, VOGEL S C. Texture measurements on quartz single crystals to validate coordinate systems for neutron time-of-flight texture analysis [J]. Journal of Applied Crystallography, 2023: 56: 1764−1775.

[35] GRIFFITHS M. X-ray diffraction line broadening and radiation damage [J]. Materialia, 2023, 27: 101704.

[36] MONSHI A, FOROUGHI M R, MONSHI M R. Modified Scherrer equation to estimate more accurately nano-crystallite size using XRD [J]. World Journal of Nano Science and Engineering, 2012, 2: 154−160.

[37] YOU D, ZHANG H, GANORKAR S, KIM T, SCHROERS J, VLASSAK J J, LEE D. Electrical resistivity as a descriptor for classification of amorphous versus crystalline phases of alloys [J]. Acta Materialia, 2022, 231: 117861.

[38] KOK M, AL-JAF A O A, CIRAK Z D, QADER I N, OZEN E. Effects of heat treatment temperatures on phase transformation, thermodynamical parameters, crystal microstructure, and electrical resistivity of NiTiV shape memory alloy [J]. Journal of Thermal Analysis and Calorimetry, 2020, 139: 3405−3413.

[39] SUNDQVIST B, TOLPYGO V K. Saturation and pressure effects on the resistivity of titanium and two Ti−Al alloys [J]. Journal of Physics and Chemistry of Solids, 2018, 122: 41−50.

[40] SHOJAEI M, KHAYATI G, KHORASANI S M, HERNASHKI R K. Investigation of spring back phenomenon in the 316L stainless steel cathode blank based on the changes in electrical resistivity and magnetic properties due to the residual stress and martensite phase formation: An industrial failure [J]. Engineering Failure Analysis, 2021, 126: 105473.

[41] ABRAHAM S T, BHAT S S. Crystal plasticity finite element modelling on the influence of grain size and shape parameters on the tensile stiffness and yield strength [J]. Materials Science and Engineering A, 2023, 877: 145155.

[42] HARSHAVARDHANA N, SIVAM S P, KUMAR G, SAXENA A K. A comparative study on misorientations to determine the extent of recrystallization in pure ETP copper [J]. Physics of Metals and Metallography, 2021, 122: 1279−1287.

[43] SHI Xiao-hui, ZHANG Qi, ZHEN Jing, FAN Zhi-yuan, LIU Jiang-lin, QIAO Jun-wei. Strengthening behavior and model of ultra-high strength Ti−15Mo−2.7Nb−3Al−0.2Si titanium alloy [J]. Transactions of Nonferrous Metals Society of China, 2024, 34: 1136−1149.

[44] YAN Xu-dong, XU Xiao-feng, ZHAO Yang, ZHOU Ya-chong, WEI Lai, WU Zhi-cheng, YU Yong-qiang, WU Chao. Achieving low elastic modulus, excellent work hardening and high corrosion resistance in Ti−6Al−4V−5.6 Cu alloy [J]. Journal of Alloys and Compounds, 2023, 959: 170582.

[45] ZHOU B, BIELER T R, LEE T K, LIU Wen-jun. Characterization of recrystallization and microstructure evolution in lead-free solder joints using EBSD and 3D-XRD [J]. Journal of Electronic Materials, 2013, 42: 319−331.

[46] ZHANG Yue, WANG Shu-yan, XU Guang-tao, WANG Gang, ZHAO Ming-hao. Effect of Microstructure on Fatigue-crack Propagation of 18CrNiMo7-6 high-strength Steel [J]. International Journal of Fatigue, 2022, 163: 107027.

[47] SHU Yan-kai, WANG Zi-yi, YANG Hong, CHEN Xian-hua, BAI Jing-ying, PAN Fu-sheng. Optimized method for the identification of slip directions in Mg alloy based on intragranular misorientation axes analysis [J]. Journal of Materials Research and Technology, 2023, 23: 6140−6149.

[48] RUI Shao-shi, SHANG Yi-bo, FAN Ya-nan, HAN Qi-nan, NIU Li-sha, SHI Hui-ji, HASHIMOTO K, KOMAI N. EBSD analysis of creep deformation induced grain lattice distortion: A new method for creep damage evaluation of austenitic stainless steels [J]. Materials Science and Engineering A, 2018, 733: 329−337.

[49] WU Chao, ZHAO Yang, XU Xiao-feng, ZHOU Ya-chong, YAN Xu-dong, WU Zhi-cheng, WE Lai, QIU Xiao-ming. Electropulse-induced texture elimination and ⟨100⟩ texture formation in hot-rolled annealed 35CrMo steel [J]. Journal of Materials Research and Technology, 2023, 24: 1537−1546.

[50] ZHAO Yun-dong, NING Rui, LI Hao, SUN Si-bo, WANG Hai-zhen, GAO Yuan, ZHAO De-qiang, CAO Xing-zhong, GAO Zhi-yong, CAI Wei. Irradiation engineered lattice distortion in Ti−Ni shape memory alloy achieving enhanced elastocaloric effect [J]. Journal of Alloys and Compounds, 2022, 906: 164280.

[51] CHAMAKURA J N, RIEMSLAG A C, REINTON T E,

POPOVICH V A, SIETSMA J. The quantitative relationship between non-linear stress-strain behaviour and dislocation structure in martensitic stainless steel [J]. Acta Materialia, 2022, 240: 118364.

[52] BRANDL E, SCHOBERTH A, LEYENS C. Morphology, microstructure, and hardness of titanium (Ti−6Al−4V) blocks deposited by wire-feed additive layer manufacturing (ALM) [J]. Materials Science and Engineering A, 2012, 532: 295−307.

[53] ZHANG Jing-wen, YU Li-ming, GAO Qiu-zhi, LIU Chen-xi, MA Zong-qing, LI Hui-jun, LIU Yong-chang, WANG Hui. Creep behavior, microstructure evolution and fracture mechanism of a novel martensite heat resistance steel G115 affected by prior cold deformation [J]. Materials Science and Engineering A, 2022, 850: 143564.

[54] XU Jian, ZHENG Jie, LIU Wan-er, HUANG You-wang, YAN Zhao-ming, ZHANG Zhi-min, WANG qiang, XUE Hong-qian. Recrystallization behavior and strengthening mechanism of extruded Mg−Gd−Y−Zn−Zr alloy with different pre-aged states [J]. Transactions of Nonferrous Metals Society of China, 2024, 34: 480−503.

[55] MENG Ling-jian, YIN Hong-liang, YAN Zhu, CUI Xiao-lei, PENG Lin. Microstructural evolution and formability of Ti−6Al−4V alloy sheet during electropulsing-assisted bending [J]. Transactions of Nonferrous Metals Society of China, 2024, 34: 519−532.

电冲击处理对 Ti−8Al−1Mo−1V 合金显微组织演变和力学性能的影响

周健[1,2]，姚宇鹏[1,2]，孙洪鑫[1,2]，刘畅[1,2]，温艳[1,2]，王立强[3]，张来昌[4]，谢乐春[1,2]，华林[1,2]

1. 武汉理工大学 现代汽车零部件技术湖北省重点实验室，武汉 430070；
2. 汽车零部件技术湖北省协同创新中心，武汉 430070；
3. 上海交通大学 材料科学与工程学院 金属基复合材料国家重点实验室，上海 200240；
4. Centre for Advanced Materials and Manufacturing, School of Engineering,
Edith Cowan University, Joondalup, Perth, WA6027, Australia

摘　要：研究了电冲击处理(EST)对 Ti−8Al−1Mo−1V 合金的显微组织演变和力学性能变化的作用机理。结果表明，EST 导致针状次生 α_s 相向 β 相转变。当 EST 时间为 0.12 s 时，针状马氏体相(α_M)析出。电子背散射衍射(EBSD)结果表明，EST 后平均晶粒尺寸从 3.95 μm 减小到 2.53 μm，表明晶粒得到细化，并发生显著的再结晶行为和马氏体相变。取向分布表明，相变引起晶体取向变化，织构分布更加均匀。压缩断裂行为表明，EST 显著提高屈服强度，同时降低断裂应变。屈服强度的提高主要归因于马氏体相的析出。所有结果表明，EST 是调控钛合金显微组织和优化织构分布的有效方法。

关键词：电冲击处理(EST)；钛合金；晶粒尺寸；织构分布；Ti−8Al−1Mo−1V

(Edited by Bing YANG)